Collective excitations in symmetric *p*-type GaAs/$Al_xGa_{1-x}As$ quantum wells

Shun-Jen Cheng and Rolf R. Gerhardts
Max-Planck-Institut für Festkörperforschung, Heisenbergstraße 1, D-70569 Stuttgart, Germany
(Received 28 September 2000; published 2 January 2001)

We present a calculation of the collective plasmon excitations in *p*-type GaAs/$Al_xGa_{1-x}As$ quantum wells that is based on the random-phase approximation and, within the $\mathbf{k}\cdot\mathbf{p}$ model takes exactly into account band-structure effects and the strong dependence of the subband wave functions on the in-plane wave vector. For symmetrically modulation-doped wells, the subband structure in the Hartree approximation, plasmon dispersions, single-particle excitations, and energy-loss spectra at zero temperature are consistently calculated. In contrast to the corresponding *n*-type quantum wells, a multisubband approximation yields a strong coupling of the intra- and intersubband plasmons, even in symmetrical wells, and predicts the existence of an additional intersubband plasmon at finite wave vectors. These drastic differences between electron and hole quantum wells are attributed to the finite overlap between eigenfunctions belonging to different subbands and different in-plane wave vectors, which exists in hole but not in electron systems.

DOI: 10.1103/PhysRevB.63.035314 PACS number(s): 73.21.Fg, 73.20.Mf, 78.66.−w

I. INTRODUCTION

Collective excitation modes (plasmons) in quasi-two-dimensional (Q2D) electron[1–5] and hole[6–8] systems characterize the optical response of these systems and have been studied experimentally by inelastic light scattering or far-infrared absorption for decades. Recently, it was found that plasmons also play an important role for the dynamical screening or enhancement of interlayer particle interactions in Coulomb drag experiments. The Coulomb drag effect in *electron* double layers in the presence and in the absence of a perpendicular magnetic field has been studied extensively in recent years, both experimentally and theoretically (for a recent review see Ref. 9). Experiments on *hole* double layers, on the other hand, have been presented only recently.[10] Characteristic differences between hole and electron double layers have been reported and traced back to the more complicated band structure of the hole systems. A detailed theory of the frictional drag in coupled hole quantum wells, including, e.g., dynamical screening effects in single and/or double quantum wells, is, however, not available. In this situation, and as a possible ingredient of such a theory, the theoretical understanding of the collective excitations in the hole systems becomes especially important. However, up to now most theoretical investigations[11–16] of collective excitations focus on the electron systems, in which the energy bands are parabolic and the wave functions $\Psi_{l,\mathbf{k}}(\mathbf{r},z)$ factorize into an in-plane part $\exp(\imath\mathbf{k}\cdot\mathbf{r})$ and a subband function $\psi_{l,\mathbf{k}}(z)$, which is independent of the in-plane wave vector $\mathbf{k}$. Here z denotes the direction perpendicular to the quantum well and $\mathbf{r}=(x,y)$ the in-plane position. These simplifications are explicitly exploited in Refs. 11–16. In *p*-type quantum wells, however, the band structure is strongly nonparabolic and the subband wave functions $\psi_{l,\mathbf{k}}(z)$ of holes strongly depend on $\mathbf{k}$ due to the coupling between valence subbands.[17] Therefore, the methods that have been developed for the calculation of plasmons in electron quantum wells are not appropriate for hole systems. Previous plasmon calculations for two-dimensional hole systems,[18] on the other hand, have been restricted to intrasubband plasmons or to vertical intersubband excitations ($\mathbf{q}=\mathbf{0}$).

In a recent communication,[19] we have presented preliminary theoretical results on the collective excitations in hole quantum wells for a simplified isotropic model, i.e., the axial approximation that neglects the warping of the band structure. In the present paper, we discuss in some detail our theoretical method for the calculation the collective excitations in the hole quantum wells, which is developed in the framework of the random-phase approximation (RPA), and is able to take, within a $4\times4\,\mathbf{k}\cdot\mathbf{p}$ calculation, the full anisotropy, the nonparabolicity and the dependence of the wave functions on $\mathbf{k}$ correctly into account. As in most of the previous works, we use the self-consistent field version of the RPA and consider only longitudinal fields described by scalar potentials.[20] As a test of our method, we first apply it to the case of an *electron* system with nearly parabolic bands, and recover the known results: the inter- and intrasubband plasmons in symmetric *n-type* quantum wells are decoupled, and (due to the minor effect of the finite well width[14]) the intrasubband plasmon dispersion is well approximated by the dispersion relations for the ideal two-dimensional electron system in the long-wavelength limit. Thus, the effective plasmon mass is close to the cyclotron mass. Then, applying our method to *p-type* quantum wells, we show that the intra- and intersubband plasmons now are intrinsically coupled (due to the dependence of the wave functions on $\mathbf{k}$) even in the symmetric structures. As a consequence, the plasmon masses are affected and are much heavier than the cyclotron masses. We also find that, at finite $\mathbf{k}$, the hybridization of wave functions between adjacent valence subbands in the Q2D hole systems leads to the occurrence of *two branches* of the intersubband plasmons, whereas electron systems have only one. One of them has only weakly $\mathbf{q}$-dependent frequencies slightly above the region of single-particle excitations (SPE's), which may be lowered and thus damped due to the coupling to higher subband excitations. The other plasmon branch, unlike usual intersubband plasmons, exhibits a strongly $\mathbf{q}$ dependent dispersion and appears only at finite $\mathbf{q}$. Both these features

originate from the hybridization of wave functions between adjacent valence subbands at finite **k**, which leads to a strong **k**-dependence of the subband wave functions $\hat{\psi}_{l,\mathbf{k}}(z)$ and a finite overlap between $\hat{\psi}_{l,\mathbf{k}}(z)$ with different l and **k**.

The aim of this paper is to emphasize the typical differences between the collective excitations in hole quantum wells and those in electron quantum wells, which result from the strong nonparabolicity and the **k** dependence of the wave functions in the hole systems. To this end, we want to keep the formalism as simple as possible, and we neglect, e.g., exchange and correlation effects as well as spin density excitations. We do, however, calculate the band structure of the quantum wells within the Hartree approximation, in order to treat the ground state and linear response consistently.

In the next section, we present our theoretical approach in some detail. First, we introduce our model and notation. Then, we define and evaluate a suitable dielectric matrix that determines screening and plasmon modes in the *p*-type Q2D systems. Based on this theory, we also investigate the energy-loss spectra. In Sec. III, we apply our approach first to the symmetric *n*-type GaAs/Al_xGa_{1-x}As quantum wells in order to compare the results with those obtained by the methods of Refs. 11–15. Then, we present our results for symmetric *p*-type GaAs/Al_xGa_{1-x}As quantum wells, including the plasmon dispersions, single-particle excitations, and energy-loss spectra. The difference between the electron and hole plasmons will be discussed in detail. The effects of the nonparabolicity, anisotropy, and dependence of the wave functions on **k** will be quantitatively evaluated.

II. THEORY

A. Electronic structure of quantum wells

We use the 4×4 Luttinger $\mathbf{k}\cdot\mathbf{p}$ model to calculate the band structure of *p*-type GaAs/Al_xGa_{1-x}As quantum wells. The wave function of a particle in the state $(l,\mathbf{k})$, where l is a subband index and $\mathbf{k}=(k_x,k_y)$ an in-plane wave vector, is expressed as $\hat{\Psi}_{l,\mathbf{k}}(\mathbf{r},z)=(1/\sqrt{A})e^{\imath\mathbf{k}\cdot\mathbf{r}}\hat{\psi}_{l,\mathbf{k}}(z)$, where A is the area of the sample. The envelope function $\hat{\psi}_{l,\mathbf{k}}$ in the basis of $J=\frac{3}{2}$ states has the form

$$\hat{\psi}_{l,\mathbf{k}}(z)=\begin{bmatrix} g_1^{l,\mathbf{k}}(z)\\ g_2^{l,\mathbf{k}}(z)\\ g_3^{l,\mathbf{k}}(z)\\ g_4^{l,\mathbf{k}}(z)\end{bmatrix}=\sum_n f_n(z)\begin{bmatrix} c_{1,n}^{l,\mathbf{k}}\\ c_{2,n}^{l,\mathbf{k}}\\ c_{3,n}^{l,\mathbf{k}}\\ c_{4,n}^{l,\mathbf{k}}\end{bmatrix}, \tag{1}$$

where the components are ordered with respect to the magnetic quantum number according to $m_J=(+3/2,-1/2,+1/2,-3/2)$. The right-hand side of Eq. (1) indicates, for later use, the expansion of the z dependence with respect to an orthonormal basis $\{f_n\}$. The expansion coefficients $\{c_{j,n}^{l,\mathbf{k}}\}$ form four-vectors $\hat{c}_n^{l,\mathbf{k}}$. Luttinger's $4\times4\,\mathbf{k}\cdot\mathbf{p}$ Hamiltonian can be written as[17,21]

$$\hat{H}=\begin{bmatrix} H_h+V(z) & c & b & 0\\ c^* & H_l+V(z) & 0 & -b\\ b^* & 0 & H_l+V(z) & c\\ 0 & -b^* & c^* & H_h+V(z)\end{bmatrix}, \tag{2}$$

where

$$H_h=-\frac{\hbar^2}{2m_0}k_z(\gamma_1-2\gamma_2)k_z-\frac{\hbar^2k^2}{2m_0}(\gamma_1+\gamma_2)+E_v(z),$$

$$H_l=-\frac{\hbar^2}{2m_0}k_z(\gamma_1+2\gamma_2)k_z-\frac{\hbar^2k^2}{2m_0}(\gamma_1-\gamma_2)+E_v(z),$$

$$b=\frac{\sqrt{3}\hbar^2}{2m_0}k_-(\gamma_3k_z+k_z\gamma_3), \tag{3}$$

$$c=\frac{\sqrt{3}\hbar^2}{4m_0}[(\gamma_2+\gamma_3)k_-^2+(\gamma_2-\gamma_3)k_+^2].$$

Here, $k_z=-\imath\partial/\partial z$, $k_\pm=k_x\pm ik_y$, $k^2=k_x^2+k_y^2$, and γ_i and E_v are the position-dependent Luttinger parameters and the valence-band edge, respectively. In the axial approximation,[22] the last term with parameter $(\gamma_2-\gamma_3)$ of c in Eq. (3) is ignored to obtain an approximate isotropic band structure in the k_x-k_y plane. An external or internal (Hartree) electrostatic potential energy $V(z)$ is considered and added to the diagonal terms. The energy of the state $(l,\mathbf{k})$ can be obtained by solving

$$\hat{H}\hat{\psi}_{l,\mathbf{k}}=E_{l,\mathbf{k}}\hat{\psi}_{l,\mathbf{k}}. \tag{4}$$

Taking the band edge in the well as energy zero, we have

$$E_v(z)=\begin{cases}0, & \text{for } |z|<w/2\\ \Delta E_v, & \text{for } |z|>w/2\end{cases} \tag{5}$$

where ΔE_v is the band edge discontinuity and w the well width. For simplicity, we neglect the difference of the values of the γ_i (and thus of the hole masses) between barrier and well, and we take the values for the well in our calculations. The internal electrostatic potential due to the distribution of charges is taken into account in the Hartree approximation. The Hartree potential $V(z)$ satisfies Poisson's equation,

$$\frac{d^2}{dz^2}V(z)=\frac{4\pi e^2}{\kappa}[\rho_h(z)-N_A^-(z)+N_D^+(z)], \tag{6}$$

where κ is the background dielectric constant. We neglect the difference of the κ values between well and barrier, and take the GaAs value $\kappa=13.1$. N_A^- (N_D^+) is the number density of occupied acceptor (empty donor) states and ρ_h is the hole density, given by

$$\rho_h(z)=\sum_{l,\mathbf{k}}\sum_{j=1}^{4}|g_j^{l,\mathbf{k}}(z)|^2[1-\mathcal{F}(E_{l,\mathbf{k}};E_F,T)],$$

$$l\in\text{valence band}, \tag{7}$$

where $\mathcal{F}$ denotes the Fermi-Dirac distribution function and E_F is the Fermi energy.

In our calculations, we assume no donor impurities, $N_D^+ \equiv 0$, and two doped layers with acceptor impurities that compensate the charge of all free carries (holes) and are located symmetrically on the both sides of the well,

$$N_A^-(z) = \frac{N_A}{2}\delta(z-d/2) + \frac{N_A}{2}\delta(z+d/2), \tag{8}$$

where $d(>w$, sufficiently large) is the distance between the two acceptor planes, and $N_A = \int dz \rho_h(z)$ equals the fixed value of the areal density of holes in the quantum well.

To solve Eq. (4) self-consistently, we follow the algorithm in Ref. 23. We expand envelope functions in terms of a suitable set of basis functions $\{f_n\}$, as indicated in Eq. (1). Since we take constant values for the Luttinger parameters γ_i, the envelope functions and their derivatives with respect to z will be continuous at the well edges, and the expansion will converge rapidly even if we work with continuous basis functions $f_n(z)$.

Expanding the matrix elements $H_{i,j}$ of the $\mathbf{k}\cdot\mathbf{p}$ Hamiltonian in Eq. (2) in the same basis, $\langle m|H_{i,j}|n\rangle \equiv \int dz f_m^*(z) H_{i,j} f_n(z)$, we have, according to Eqs. (1) and (4),

$$\sum_n \sum_{j=1}^{4} \langle m|H_{i,j}|n\rangle c_{j,n}^{l,\mathbf{k}} = E_{l,\mathbf{k}} c_{i,m}^{l,\mathbf{k}}. \tag{9}$$

Solving this eigenvalue problem, we can obtain the eigenvalues $E_{l,\mathbf{k}}$ and expansion coefficients $[c_{j,n}^{l,\mathbf{k}}]$ of the eigenfunctions, which yield the Fermi energy and hole density according to Eq. (7), and from the solution of Poisson's equation the new result for the Hartree potential, which enters the next iteration step.

In the actual calculations we use, in contrast to Ref. 23, the plane-wave basis

$$f_n(z) = \frac{\exp(\imath k_n z)}{\sqrt{L}}, \quad k_n \equiv \frac{2\pi n}{L}, \quad n = 0, \pm 1, \pm 2, \ldots, \tag{10}$$

on the interval $|z| < L/2$, where $L > w$ is taken so large that for the subbands of interest the functions $g_j^{l,\mathbf{k}}(z)$ are sufficiently small at $|z| \sim L/2$, but small enough to avoid an unnecessarily large basis set. (Note that in this basis the Hamiltonian matrix elements are Fourier coefficients.) We took $L \approx 2w$ and achieved with 21 basis functions ($|n| \leqslant 10$) satisfying results. In the self-consistent calculation convergence is assumed when the relative variation of the values of the Fourier coefficients of $V(z)$ and $\psi(z)$ between subsequent iterations is less than 2%. The above algorithm is also used for the $6\times 6\,\mathbf{k}\cdot\mathbf{p}$ calculation in Sec. III and may also be extended straightforwardly to other multiband $\mathbf{k}\cdot\mathbf{p}$ models.

B. Screening and dielectric function

We expose the quantum well to an external, harmonic longitudinal electric field with an in-plane wave vector $\mathbf{q} = (q_x, q_y)$ and frequency ω, which polarizes the system. Thus, the screened (or self-consistent) potential in the system, $V_{\mathbf{q},\omega}^{sc}(\mathbf{r},z,t) = V_{\mathbf{q},\omega}^{sc}(\mathbf{r},z)e^{-\imath\omega t} = V_{\mathbf{q},\omega}^{sc}(z)e^{\imath(\mathbf{q}\cdot\mathbf{r}-\omega t)}$, is the sum of the external potential $V_{\mathbf{q},\omega}^{ex}(\mathbf{r},z,t)$ and $V_{\mathbf{q},\omega}^{ind}(\mathbf{r},z,t)$, which is induced by polarization. In the spirit of the RPA, we replace the response of the Coulomb-interacting hole system to the external potential by the response of the noninteracting system to the self-consistent field $V_{\mathbf{q},\omega}^{sc}(\mathbf{r},z,t)$. The charge density induced by $V_{\mathbf{q},\omega}^{sc}$ can be calculated according to standard linear response theory.[20] It has the form $n_{\mathbf{q},\omega}^{ind}(\mathbf{r},z,t) = n_{\mathbf{q},\omega}^{ind}(z)e^{\imath(\mathbf{q}\cdot\mathbf{r}-\omega t)}$, and can be written as

$$n_{\mathbf{q},\omega}^{ind}(z) = \int dz' \Pi(z,z';\mathbf{q},\omega) V_{\mathbf{q},\omega}^{sc}(z'), \tag{11}$$

where the polarizability has the form

$$\Pi(z,z';\mathbf{q},\omega) = \lim_{\gamma\to 0} \sum_{1,2} \delta_{\mathbf{k}_2,\mathbf{k}_1+\mathbf{q}} \hat{\psi}_1^\dagger(z)\hat{\psi}_2(z) \times \frac{\mathcal{F}(E_1)-\mathcal{F}(E_2)}{E_1 - E_2 + \hbar\omega + \imath\gamma} \hat{\psi}_2^\dagger(z')\hat{\psi}_1(z'). \tag{12}$$

Here the subscripts $i(=1,2)$ denote the states $(l_i, \mathbf{k}_i)$ and $\hat{\psi}^\dagger$ denotes the adjoint (complex conjugate and transposed) of (the four-vector) $\hat{\psi}$, which reduces to the complex conjugate if $\hat{\psi}$ is scalar (one-band model). Instead of taking the limit $\gamma \to 0$, we may consider a finite but small value of the phenomenological damping parameter γ to model scattering effects. The induced density determines the induced potential,

$$V_{\mathbf{q},\omega}^{ind}(z) = \int dz' W_q(z-z') n_{\mathbf{q},\omega}^{ind}(z'), \tag{13}$$

where the Green's function of Poisson's equation, $W_q(z-z') = v_q \exp(-q|z-z'|)$ with $v_q = 2\pi e^2/(\kappa q)$ represents the Coulomb interaction. Since $V_{\mathbf{q},\omega}^{ex}(z) = V_{\mathbf{q},\omega}^{sc}(z) - V_{\mathbf{q},\omega}^{ind}(z)$, we can express the external potential in terms of the screened one,

$$V_{\mathbf{q},\omega}^{ex}(z) = \int dz' \epsilon_{\mathbf{q},\omega}(z;z') V_{\mathbf{q},\omega}^{sc}(z'), \tag{14}$$

which defines the dielectric function

$$\epsilon_{\mathbf{q},\omega}(z;z') = \delta(z-z') - \int d\bar{z} W(z-\bar{z}) \Pi(\bar{z},z';\mathbf{q},\omega) \tag{15}$$

of our Q2D system. Note that $\Pi(\bar{z},z';\mathbf{q},\omega)$ is nonzero only if both arguments $\bar{z}$ and z' are located in the area of the quantum well, where the wave functions are finite. The same holds for the z' integrals in Eqs. (13) and (14), but not for the z dependence in Eqs. (13)–(15), which is asymptotically $\propto \exp(-q|z|)$ and decays only slowly for small q.

For the calculation of collective excitations and of absorption spectra, one needs the determinant and the inverse of the operator $\epsilon_{\mathbf{q},\omega}(z;z')$, respectively. For an efficient evaluation of these quantities, it is useful to expand $\epsilon_{\mathbf{q},\omega}(z;z')$ in terms

of a suitable, preferably small set of basis functions. It is the choice of this basis in which our approach differs from the previous ones.[11,13]

1. Excitation basis

In order to clarify this difference and for later comparison of the results, we first recall the conventional approach in a slightly generalized form.[11,13] We expand the subband wave functions with respect to the basis indicated in Eq. (1). [In the parabolic approximation for the conduction band, where the subband functions $\hat{\psi}_{l,\mathbf{k}}(z)$ are scalars independent of $\mathbf{k}$, these may be taken as basis functions, $f_n(z)=\hat{\psi}_{n,\mathbf{k}}(z)$, so that the expansion coefficients in Eq. (1) become $c_n^{l,\mathbf{k}}=\delta_{l,n}$, independent of $\mathbf{k}$.] We insert this expansion into Eq. (12) and take matrix elements of Eq. (14), to obtain with the notation $\langle m|V^{ex}_{\mathbf{q},\omega}|n\rangle=V^{ex}_{m,n}$,

$$V^{ex}_{m,n}=\sum_{m',n'}\epsilon_{m,n;m',n'}V^{sc}_{m',n'}, \tag{16}$$

where the subscripts $\mathbf{q},\omega$ have been suppressed for brevity. The dielectric matrix is obtained from Eqs. (14)–(16) as

$$\epsilon_{m,n;m',n'}=\delta_{m,m'}\delta_{n,n'}-\sum_{\bar{m},\bar{n}} v_{m,n;\bar{m},\bar{n}}\Pi_{\bar{m},\bar{n};m',n'} \tag{17}$$

with

$$v_{m,n;\bar{m},\bar{n}}=\int dz\int d\bar{z}f^*_m(z)f_n(z)W_q(z-\bar{z})f^*_{\bar{m}}(\bar{z})f_{\bar{n}}(\bar{z}) \tag{18}$$

the Coulomb matrix element in this basis,[11,13] and with the generalized polarizability function

$$\Pi_{m,n;m',n'}=\sum_{l,l',\mathbf{k}}[\hat{c}^{l,\mathbf{k}}_m]^\dagger\hat{c}^{l',\mathbf{k}+\mathbf{q}}_n \times\frac{\mathcal{F}(E_{l,\mathbf{k}})-\mathcal{F}(E_{l',\mathbf{k}+\mathbf{q}})}{E_{l,\mathbf{k}}-E_{l',\mathbf{k}+\mathbf{q}}+\hbar\omega+\imath\gamma}[\hat{c}^{l',\mathbf{k}+\mathbf{q}}_{m'}]^\dagger\hat{c}^{l,\mathbf{k}}_{n'}, \tag{19}$$

which contains the expansion coefficients introduced in Eq. (1). The condition for plasmon modes is the vanishing of the determinant of the dielectric matrix, $\det[\epsilon_{m,n;m',n'}]=0$.

For the parabolic approximation of the conduction band, $c_n^{l,\mathbf{k}}=\delta_{l,n}$, Eq. (19) simplifies to

$$\Pi^{\mathrm{par}}_{m,n;m',n'}=\delta_{n',m}\delta_{m',n}\sum_{\mathbf{k}}\frac{\mathcal{F}(E_{m,\mathbf{k}})-\mathcal{F}(E_{n,\mathbf{k}+\mathbf{q}})}{E_{m,\mathbf{k}}-E_{n,\mathbf{k}+\mathbf{q}}+\hbar\omega+\imath\gamma}, \tag{20}$$

and the matrix elements $V_{m,n}$ indicate excitations between the subbands n and m. If only one subband is partially occupied, say that with the wave function $\hat{\psi}_1(z)$, $\Pi^{\mathrm{par}}_{m,n;m',n'}$ is nonzero only if at least one of the indices m,n is 1. If only the low-energy transitions between the partially occupied subband and the adjacent subband are considered, only the matrix elements $V_{1,1}$, $V_{1,2}$, and $V_{2,1}$ enter Eq. (16), and $\epsilon_{m,n;m',n'}$ reduces to the 3×3 matrix discussed in the literature.[11,13] If more transitions have to be considered since higher bands are partially occupied or higher excitation energies become important, the excitation representation may become inconvenient since the dimension of the dielectric matrix becomes too large.

2. Plane-wave Fourier basis

If the subband functions $\hat{\psi}_{l,\mathbf{k}}(z)$ really depend on $\mathbf{k}$, as for the hole quantum wells of our interest, they cannot be used to build such an excitation basis. Then we explicitly use the basis defined in Eq. (10) and exploit the fact that the potential matrix elements reduce to the Fourier coefficients

$$V^{ex}_{m,n}=\int_{-L/2}^{L/2}\frac{dz}{L}e^{\imath(k_n-k_m)z}V^{ex}_{\mathbf{q},\omega}(z)\equiv V^{ex}_{m-n}, \tag{21}$$

of the plane-wave Fourier expansion $V^{ex}_{\mathbf{q},\omega}(z)=\sum_m\exp(\imath k_m z)V^{ex}_m$ of the external potential in the well region. With the analogous expansion of $V^{sc}_{\mathbf{q},\omega}(z)$, the Fourier transform of Eq. (14) becomes

$$V^{ex}_m=\sum_n\epsilon^{\mathbf{q},\omega}_{m,n}V^{sc}_n \tag{22}$$

with

$$\epsilon^{\mathbf{q},\omega}_{m,n}=\frac{1}{L}\int_{-L/2}^{L/2}dz\int_{-L/2}^{L/2}dz'e^{-\imath k_m z}\epsilon(z,z')e^{\imath k_n z'}. \tag{23}$$

This again has the structure

$$\epsilon^{\mathbf{q},\omega}_{m,n}=\delta_{m,n}-\sum_{m'}v^q_{m,m'}\Pi^{\mathbf{q},\omega}_{m',n}, \tag{24}$$

where $v^q_{m,n}$ and $\Pi^{\mathbf{q},\omega}_{m,n}$ are the Fourier transforms calculated as in Eq. (23), but with $\epsilon(z,z')$ replaced by $W_q(z-z')$ and $\Pi(z,z';\mathbf{q},\omega)$, respectively. The matrices in this plane-wave Fourier representation are related to those in the excitation representation of Sec. II B 1 by

$$v_{m,n;m',n'}=(1/L)v^q_{m-n,n'-m'},$$

$$\Pi^{\mathbf{q},\omega}_{m,n}=(1/L)\sum_{m',n'}\Pi_{m',m'+m;n'+n,n'}, \tag{25}$$

$$\epsilon^{\mathbf{q},\omega}_{m,n}=\sum_{n'}\epsilon_{m+m',m';n+n',n'}.$$

(Here the last expression does not depend on the arbitrary value of m'.) Now the dispersion relations of the collective excitations are determined by the zeros of the determinant of the dielectric matrix defined by Eq. (23), $\det[\epsilon^{\mathbf{q},\omega}_{m,n}]=0$.

C. Energy-loss spectra

The average power dissipation per unit area in the screened system is given by

$$\overline{P} = \frac{1}{2A}\mathrm{Re}\int d^3r[\mathbf{E}^{sc}(\mathbf{r},z)]^* \cdot \mathbf{J}^{ind}(\mathbf{r},z), \tag{26}$$

where $\mathbf{E}^{sc}(\mathbf{r},z) = -\boldsymbol{\nabla} V^{sc}_{\mathbf{q},\omega}(\mathbf{r},z)/e$ is the amplitude of the dynamical self-consistent electric field (with e the charge of a hole). The induced current density, $\mathbf{J}^{ind}(\mathbf{r},z;t) = \mathbf{J}^{ind}(\mathbf{r},z)\exp(-\imath\omega t)$ satisfies the continuity equation $\nabla\cdot\mathbf{J}^{ind}(\mathbf{r},z;t) + e(\partial/\partial t)n^{ind}(\mathbf{r},z;t) = 0$, where $n^{ind}(\mathbf{r},z;t) = n^{ind}_{\mathbf{q},\omega}(z)\exp[\imath(\mathbf{q}\cdot\mathbf{r} - \omega t)]$. Thus, Eq. (26) can be integrated by parts and written as

$$\overline{P} = -\frac{\omega}{2}\mathrm{Im}\int dz[V^{sc}_{\mathbf{q},\omega}(z)]^* n^{ind}_{\mathbf{q},\omega}(z)$$

$$= -\frac{\omega}{2}L\ \mathrm{Im}\sum_n\ (V^{sc}_n)^* n^{ind}_n, \tag{27}$$

where n^{ind}_n is the Fourier component of $n^{ind}_{\mathbf{q},\omega}(z)$. Here we have exploited the fact that (after integrating by parts) only the region near the quantum well, where $n^{ind}_{\mathbf{q},\omega}(z)$ is nonzero, contributes to the z integral, and our plane-wave Fourier expansion can be applied. Next we use the Fourier transformation of Eq. (13), $V^{ind}_m = \Sigma_n v^q_{m,n} n^{ind}_n$, to express n^{ind}_n in terms of the Fourier coefficients $V^{ind}_n = V^{sc}_n - V^{ex}_n$. From the definitions given in Eq. (23) and below, it is easily seen that the matrix $v^q_{m,n}$ is real and symmetric. The same holds for its inverse with the matrix elements $[v^{-1}(q)]_{m,n}$ (see Appendix A for explicit results). Therefore, the quadratic term in V^{sc}_n does not contribute to the imaginary part in Eq. (27). Finally, in the term containing $(V^{sc}_m)^*$ and V^{ex}_n, we express V^{sc}_m in terms of V^{ex}_n to obtain

$$\overline{P} = \frac{\omega}{2}L\ \mathrm{Im}\sum_m \left[\sum_{\bar{m}}\ (\epsilon^{-1})_{m,\bar{m}} V^{ex}_{\bar{m}}\right]^* \left[\sum_n\ [v^{-1}(q)]_{m,n} V^{ex}_n\right]. \tag{28}$$

In order to obtain a reasonable normalization of this result, we consider only a single Fourier component of the external potential, $V^{ex}(\mathbf{r},z) = V^{ex}_n \exp(\imath[\mathbf{q}\cdot\mathbf{r} + k_n z])$ and divide the absorbed power per sample area by the field energy per area, $u_n = L|\nabla V^{ex}(\mathbf{r},z)/e|^2/(16\pi\kappa)$,[25] produced by the external field in the slab of thickness L. This can be written $u_n = L|V^{ex}_n|^2/(4\kappa^2 v^{3d}_{q_n})$, where $v^{3d}_{q_n} = 4\pi e^2/(\kappa[q^2 + k_n^2])$ is the three-dimensional Fourier component of the Coulomb interaction and has the same dimension as the matrix $v^q_{m,n}$. Exploiting the symmetry properties of the inverse matrix $[v^{-1}(q)]_{m,n}$ once more, we get the result

$$\overline{P}_n/u_n = -\omega(2\kappa^2 v^{3d}_{q_n})\mathrm{Im}\sum_m\ [v^{-1}(q)]_{n,m}(\epsilon^{-1})_{m,n}, \tag{29}$$

which has the dimension sec^{-1}. In the plots of our numerical results we omit the factor $2\kappa^2 v^{3d}_{q_n}$.

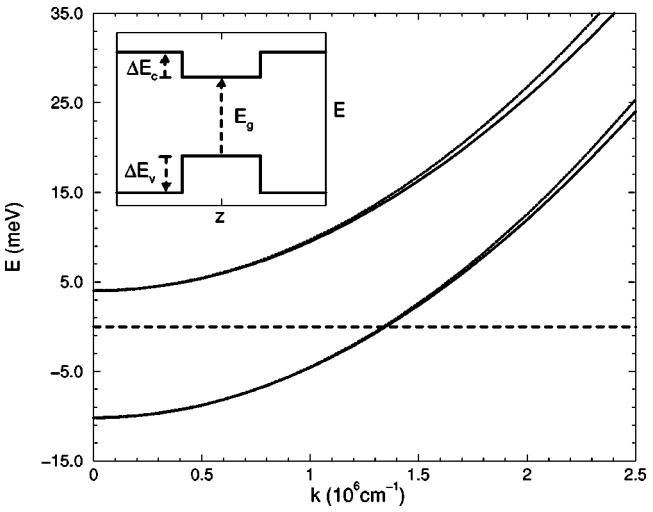

FIG. 1. Subband energies relative to the Fermi level (dashed line) for the *n*-type symmetric GaAs/$Al_{0.22}Ga_{0.78}$As quantum well of width 30 nm and electron density $N_e = 2.9\times10^{11}$ cm^{-2}. Solid lines are calculated from the $6\times6\mathbf{k}\cdot\mathbf{p}$ model. Dotted lines are parabolic bands with the effective mass $m^* = 0.067m_0$. The inset schematically shows the band edge profiles of the conduction and valence bands of the quantum well.

III. RESULTS AND DISCUSSIONS

A. *n*-type quantum wells

To verify our approach and for a later detailed comparison with the hole quantum wells, we apply the different expansion methods discussed in Sec. II first to electron quantum wells. We consider a symmetric GaAs/$Al_{0.22}Ga_{0.78}$As quantum well with the width 30 nm and the electron density $N_e = 2.9\times10^{11}$ cm^{-2}.

First, we calculate the subband structure in the one-band effective mass approximation, with $m^*_c = 0.067m_0$, where m_0 is free electron mass, and obtain subband wave functions $\psi_{l,\mathbf{k}}(z)$, which are independent of the in-plane wave vector $\mathbf{k}$. The two lowest, parabolic subbands are shown in Fig. 1 as dotted lines. Then we apply the formalism sketched in Sec. II B 1, i.e., the usual approach,[11–16] to calculate the dispersion relations of collective excitations. Since only the lowest subband is partially occupied for the chosen parameter values, we consider only the two lowest subbands in the excitation basis and obtain a 3×3 dielectric matrix $\epsilon_{m,n;m',n'}$. The results are indicated in Fig. 2 by plus signs, and fully consistent with previous work. For the symmetric electron quantum wells, the intra- and intersubband plasmons are decoupled,[14] i.e., if we consider only the lowest subband in our plasmon calculation, we obtain the same dispersion for the *intrasubband* plasmons. It has also been shown that the finite well width affects the intrasubband plasmon dispersion only slightly as $q\to0$.[14,13] So, the intrasubband plasmon dispersion in symmetric electron quantum wells can be well approximated by the plasmon frequency of the *ideal two-dimensional* electron system (2DES) in the long-wavelength limit, which is given by[13]

$$\omega_p = (2\pi N_e e^2 q/\kappa m_p)^{1/2}. \tag{30}$$

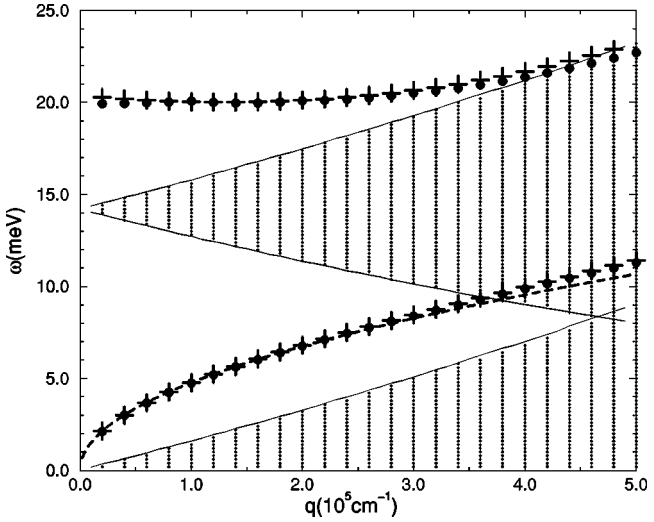

FIG. 2. Plasmon dispersions and single-particle excitations (SPE's) for the sample of Fig. 1. Filled circles: intra- (lower) and intersubband (upper) plasmon modes calculated by the approach of Sec. II B 2, with full band structure of the $6\times6\mathbf{k}\cdot\mathbf{p}$ model. The plus symbol: intra- (lower) and intersubband (upper) plasmon modes calculated by the approach of Sec. II B 1, based on the parabolic band structure and wave functions calculated with the single-band effective mass approximation with $m^*=0.067m_0$. Dashed line: ideal two-dimensional plasmon frequency $\omega_p=(2\pi N_e e^2 q/\kappa m^*)^{1/2}$. Hatched area: the inter- and intrasubband SPE.

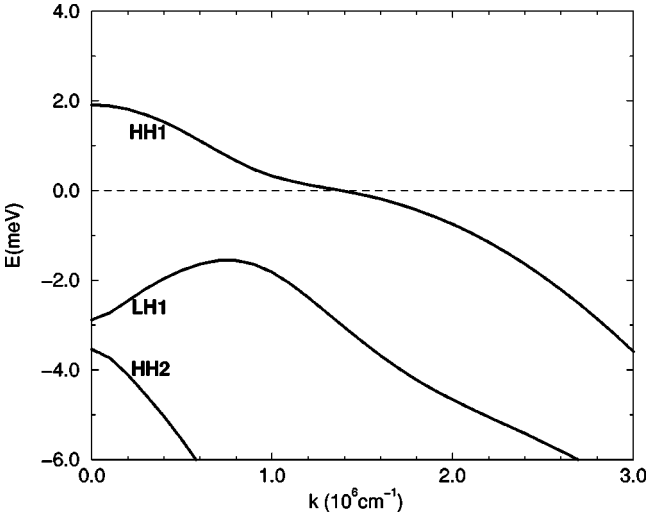

FIG. 3. Band structure for the symmetric *p*-type $GaAs/Al_{0.37}Ga_{0.63}As$ quantum well of width 22 nm and hole density $N_h=3\times10^{11}$ cm^{-2}, from the $4\times4\mathbf{k}\cdot\mathbf{p}$ flat-band model. Dashed line: Fermi level, taken as energy zero.

Here $m_p=m_c^*=0.067m_0$, i.e., for the ideal 2DES the plasmon mass, the cyclotron effective mass, and the band mass of the electrons are all identical. The ideal 2D dispersion of Eq. (30) is shown in Fig. 2 as a dashed line. The effective plasmon mass m_p for *quasi-two-dimensional* systems is defined and determined by fitting Eq. (30) to the measured or calculated curve of intrasubband plasmons. Apparently, the effective plasmon masses for symmetric electron quantum wells are very close to m_c^* (see Fig. 2).

In order to test the formalism presented in Sec. II B 2, which allows us to treat the dependence of $\psi_{l,\mathbf{k}}(z)$ on $\mathbf{k}$ and the nonparabolicity exactly within $\mathbf{k}\cdot\mathbf{p}$ theory, we then performed a second calculation based on the Kane $6\times6\mathbf{k}\cdot\mathbf{p}$ model, which is given in Ref. 26. Here we made the spherical approximation and used the following $\mathbf{k}\cdot\mathbf{p}$ parameters and values for the band offset: $m_c^*=0.067m_0$, $E_g=1.52$ eV, [24] $E_p=25.7$ eV, $\gamma_1=6.85$, $\gamma_2=\gamma_3=2.58$, $P=\sqrt{\hbar^2E_p/2m_0}$, $F=m_0/2m_c^*-E_p/3E_g-1/2$, $\Delta E_c=0.15$ eV, $\Delta E_v=-0.1$ eV. In this work, we describe the barriers only by the band edge discontinuities and assume that the other $\mathbf{k}\cdot\mathbf{p}$ parameters in the barrier have the same value as in the well. As shown in Fig. 1, the calculated $\mathbf{k}\cdot\mathbf{p}$ band structure is very close to that of the one-band parabolic model at small $\mathbf{k}$, and becomes only slightly flatter as $\mathbf{k}$ increases. At $T=0$ K, one subband of the quantum well is occupied by electrons and the two lowest subbands will be relevant in our plasmon calculations. In our numerical calculation, we use the plane-wave Fourier expansion and truncate $[\epsilon_{m,n}]$ of Eq. (23) to a $(2M+1)\times(2M+1)$ matrix, restricting the considered Fourier coefficients to $|m|\leqslant M$. For the purpose in this work, a small value of M $(\geqslant3)$ is enough to make the calculated results well converge. The calculated plasmon dispersions and the SPE's, i.e., the bare transitions between subbands obeying only energy and momentum conservation, are shown in Fig. 2 for temperature $T=0$. As usual, the SPE between band l_1 and l_2 at (q,ω) is numerically obtained by the requirement $\mathrm{Im}\,\chi\neq0$, where χ is the polarizability function and defined by $\chi\equiv\lim_{\gamma\to0}\Sigma_{\mathbf{k}}[\mathcal{F}(E_{l_1,\mathbf{k}})-\mathcal{F}(E_{l_2,\mathbf{k}+\mathbf{q}})]/(E_{l_1,\mathbf{k}}-E_{l_2,\mathbf{k}+\mathbf{q}}+\hbar\omega+\imath\gamma)$. Because the subbands are parallel for the electron system, the allowed intersubband SPE energies approach the value of the energy difference of the subbands E_{12}, as $q\to0$, i.e., the width of the SPE region shrinks to zero with $q\to0$.

The plasmon dispersions calculated from the $(2M+1)\times(2M+1)$ matrix $[\epsilon_{m,n}]$, indicated in Fig. 2 by filled circles, are very close to those obtained by the method of Refs. 11–16. This should be the case, because the nonparabolicity and dependence of the subband wave functions on $\mathbf{k}$ for the electron system are very weak, and it shows that our more general approach reproduces the known results of the excitation-basis approach in the limits of its applicability.

B. Hole quantum wells in the flat-band model

In order to manifest the basic characteristics of the collective excitations in hole systems and contrast them with those of electron systems, we first consider the hole quantum wells in a simplified model, i.e., the flat-band model in connection with the axial approximation. Results for the more realistic model including the warping and Hartree effect will be presented in the next section. Figure 3 shows the subband structure of a symmetric *p*-type $GaAs/Al_{0.37}Ga_{0.63}As$ quantum well of width $w=22$ nm and hole density $N_h=3\times10^{11}$ cm^{-2} calculated within the Luttinger $4\times4\mathbf{k}\cdot\mathbf{p}$ and flat-band model, in which the energy edge profile is piecewise-continuous by ignoring any band-bending effect due to an electrostatic potential. In this $\mathbf{k}\cdot\mathbf{p}$ calculation, we

made the axial approximation[22] to neglect warping and used the following $\mathbf{k}\cdot\mathbf{p}$ parameters and values for the valence-band offset: $\gamma_1=6.85$, $\gamma_2=2.1$, $\gamma_3=2.9$, and $\Delta E_v=-0.18$ eV [24]. Due to the subband coupling, the band shapes are nonparabolic and the subband wave functions $\hat{\psi}_{l,\mathbf{k}}(z)$ are strongly dependent on the in-plane wave vectors $\mathbf{k}$. The subband label HHn (LHn) means that the wave functions of this subband at $\mathbf{k}=0$ purely consist of heavy- (light-) hole components. However, at finite $\mathbf{k}$, the $\hat{\psi}_{l,\mathbf{k}}(z)$ are hybrids of these heavy-hole and light-hole eigenfunctions.[17] The hybridization is especially strong in the region of the anticrossing, where the energies of the subbands $HH1$ and $LH1$ come very close ($|\mathbf{k}|\sim 9\times 10^5$ cm^{-1}). Plasmon dispersions and SPE for this flat-band model are shown in Figs. 4(a) and 4(b). Since the valence subbands are not parallel (see Fig. 3), intersubband SPE's cover a wide energy region, even as $\mathbf{q}\rightarrow 0$.

1. Single-subband approximation

In the plasmon calculations, we first consider only the upper degenerate subband $HH1$ (see Fig. 3) in the l and l' summations of Eq. (19). The resulting intrasubband dispersion is shown in Fig. 4(a) by filled circles. Since the intrasubband plasmons for small q involve only excitations between the states near the Fermi edge, the intrasubband plasmon dispersion in our isotropic model can be well approximated by the ideal 2D plasmon frequency in the long-wavelength limit,[13] i.e., $\omega_p=(2\pi N_h e^2 q/\kappa m_p)^{1/2}$, provided the effective plasmon mass, m_p, is replaced by the relevant band mass near the Fermi energy, $m_c(k_F)$. This is the ''cyclotron mass'' defined by $\hbar^2 k_F/m_c(k_F)=[dE_{HH1}(k)/dk]_{k=k_F}$. Since the Fermi edge crosses the anticrossing region, where the cyclotron effective mass varies strongly with respect to k, the intrasubband plasmons can be well approximated by the frequencies of ideal 2D plasmon with plasmon mass in the range $m_c(k_F+q_{max})<m_p<m_c(k_F)$, where $m_c(k_F)\approx 1.4m_0$ and $m_c(k_F+q_{max})\approx 0.9m_0$ for $k_F\approx 1.4\times 10^6$ cm^{-1} and $q_{max}=5\times 10^5$ cm^{-1}, as shown in Fig. 4(a).

2. Two-subband approximation

Next, we include, in addition to $HH1$, the subband $LH1$ in the l and l' summations of Eq. (19). The results are shown in Fig. 4(b) as filled circles and, as compared with *n*-type quantum wells,[14] they exhibit two surprising features. First, it is found that there exists a strongly *q-dependent* intersubband plasmon that shows a positive dispersion and is damped in the SPE region for $q<2.2\times 10^5$ cm^{-1}, whereas the intersubband plasmons in the electron system are weakly q dependent. Second, the intrasubband plasmon is apparently strongly coupled to this intersubband plasmon, even though the quantum well has a symmetric structure, since its frequency is lowered and its effective mass is much heavier than the cyclotron mass $m_c(k_F)$.

To understand the origin of this plasmon feature, we expand the dielectric function in the excitation basis, as shown in Sec. II B 1, and try to obtain an analytical formulation. If

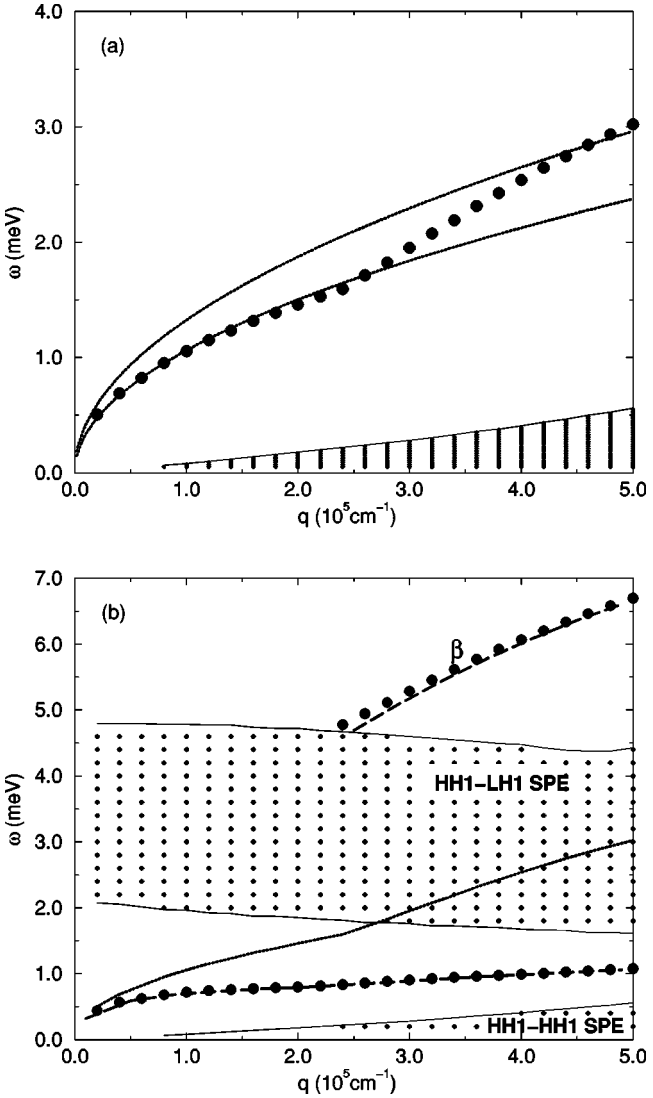

FIG. 4. Plasmon dispersions and SPE for the sample and the model of Fig. 3. (a) Filled circles: intrasubband plasmon, only highest subband $HH1$ considered. Dotted lines: ideal 2D plasmon frequency with $m_c(k=k_F=1.4\times 10^6\text{cm}^{-1})=1.4m_0$ (lower) and $m_c(k=1.9\times 10^6\text{cm}^{-1})=0.9m_0$ (upper), see text. (b) Filled circles: intra- and intersubband plasmon modes, full calculation including the two highest subbands ($HH1$,$LH1$). Dotted line: intrasubband plasmon, only highest subband $HH1$ considered, as shown in (a). Dashed line: plasmon dispersion obtained by Eq. (31); see text. Hatched area: inter- and intrasubband SPE.

we neglect the minor difference of the scalar envelope functions of the $HH1$ and $LH1$ eigenfunctions at $\mathbf{k}=0$ in the two-subband approximation (see Appendix B), the wave function is expressed as the product of a single basis function $f_1(z)$ and a four-component vector $\hat{c}_1^{l,\mathbf{k}}$, i.e., $\hat{\Psi}_{l,\mathbf{k}}(z)=f_1(z)\hat{c}_1^{l,\mathbf{k}}$, and an approximate, *scalar* dielectric function can be derived:

$$\epsilon=1-v_{1,1;1,1}\Pi_{1,1;1,1}, \tag{31}$$

where

$$\Pi_{1,1;1,1} \approx \sum_{l,l',\mathbf{k}} |\langle l,\mathbf{k}|l',\mathbf{k}+\mathbf{q}\rangle|^2 P_{l,l'}(\mathbf{k};\mathbf{q},\omega), \qquad (32)$$

$$P_{l,l'}(\mathbf{k};\mathbf{q},\omega) = \lim_{\gamma\to 0} \frac{\mathcal{F}(E_{l,\mathbf{k}}) - \mathcal{F}(E_{l',\mathbf{k}+\mathbf{q}})}{E_{l,\mathbf{k}} - E_{l',\mathbf{k}+\mathbf{q}} + \hbar\omega + \imath\gamma},$$

and $\langle l,\mathbf{k}|l',\mathbf{k}+\mathbf{q}\rangle = \int dz [\hat{\psi}_{l,\mathbf{k}}]^{\dagger}(z)\hat{\psi}_{l',\mathbf{k}+\mathbf{q}}(z) = [\hat{c}_1^{l,\mathbf{k}}]^{\dagger}\hat{c}_1^{l',\mathbf{k}+\mathbf{q}}$ (Appendix B). The calculated plasmon dispersion determined by the zeros of Eq. (31) is shown in Fig. 4(b) as dashed line.

Further analyzing Eq.(32), we notice that $\Pi_{1,1;1,1}$ contains not only the terms related to intrasubband excitations, $P_{l,l}$, but also those related to *intersubband* excitations, $P_{l,l'}$ $(l \neq l')$. Note that vertical $(\mathbf{q}=0)$ intersubband excitations between the $(HH1,s)$ and $(LH1,s')$ are not possible in this case, since, although $f_1(z)$ is the same for both states, the four-vectors are orthogonal, i.e. $[\hat{c}_1^{l,\mathbf{k}}]^{\dagger}\hat{c}_1^{l',\mathbf{k}}=0$ (see Appendix B). Therefore, there exists no intersubband plasmon for $q=0$ in Fig. 4(b). On the other hand, it is due to the finite overlap between the wave functions of different subbands and wave vectors, i.e., $\langle l,\mathbf{k}|l',\mathbf{k}+\mathbf{q}\rangle \neq 0$, that $P_{l,l'}$ for $l \neq l'$ appears in Eq. (32). In contrast to the situation met with parabolic conduction bands, the wave functions of different hole subbands are only orthogonal if they are taken at the *same* **k** value. At *different* **k** values, they are, in general, not orthogonal, and, due to the hybridization of heavy- and light-hole states, the overlap $\langle l,\mathbf{k}|l',\mathbf{k}+\mathbf{q}\rangle$ is nonzero for $\mathbf{q}\neq\mathbf{0}$ and $l \neq l'$. We expected and confirmed numerically, that this overlap increases as q increases and is especially large if the **k** values come from a region where the band structure shows strong nonparabolicities, like the anticrossing-type feature at $|\mathbf{k}| \sim 8.5\times 10^5$ cm^{-1} in Fig. 3, which indicates a strong hybridization of wave functions. The $P_{l,l'}$ $(l \neq l')$ in Eq. (32), which are absent in the dielectric function of the single-subband model, do affect the intrasubband plasmons determined in the single-subband model [Fig. 4(a)] and lead to the coupling of the intrasubband plasmons to the intersubband plasmons. On the other hand, the $P_{l,l'}$ $(l \neq l')$ lead also to zeros of $\epsilon(\mathbf{q},\omega)$, Eq. (31), at the higher frequencies of intersubband excitations, and cause the strongly **q**-dependent intersubband plasmons, denoted as β modes, if the wave function overlap, $|\langle l,\mathbf{k}|l',\mathbf{k}+\mathbf{q}\rangle|$, is sufficiently large. Since $|\langle l,\mathbf{k}|l',\mathbf{k}+\mathbf{q}\rangle|$ is strongly q dependent, vanishing at $q=0$ and increasing with increasing q, the β modes are damped as q becomes too small and appear, as q is sufficiently large, with strongly **q**-dependent frequencies. The inclusion of other higher subbands will affect again the plasmon dispersion in Fig. 4(b). But, we will not investigate this further in the simplified model.

C. Hole quantum wells within the Hartree approximation

To be consistent with the spirit of RPA, we now consider the sample with the ground state calculated in the Hartree approximation. Also, the axial approximation used so far is relaxed. Figure 5 shows the subband structure of the symmetrically modulation-doped *p*-type $GaAs/Al_{0.37}Ga_{0.63}As$ quantum well, with the same structure parameters (γ_i and valence-band offsets) as that in Fig. 3, which is self-consistently calculated within the Luttinger $4\times 4\mathbf{k}\cdot\mathbf{p}$ model and the Hartree approximation. We assumed that all free carriers (holes) come from two identically doped layers, which have the same dopant (acceptor) density and the same separation from the quantum well, as described in Eq. (8). The band structure exhibits a nonparabolic and anisotropic feature. In Fig. 5, the values of the Fermi wave vectors in the direction (100) and (110) are different. Besides, one can notice that the second highest subband in Fig. 5 is $HH2$ instead of $LH1$ in the flat-band model (see Fig. 3). For the quantum well in the flat-band model, $E_{HHn,\mathbf{k}=\mathbf{0}}/E_{LHm,\mathbf{k}=\mathbf{0}} \approx [(\gamma_1-2\gamma_2)n^2]/[(\gamma_1+2\gamma_2)m^2]$ (if the energy of the band edge is taken as zero). Therefore, $LH1$ has always higher energy than $HH2$ because $[(\gamma_1-2\gamma_2)2^2]/[(\gamma_1+2\gamma_2)]>1$ for the parameters of GaAs. It is due to the Hartree potential that the $HH2$ state (at $\mathbf{k}=\mathbf{0}$) has higher energy than $LH1$ in Fig. 5. The relaxation of the axial approximation does not affect the bound state at $\mathbf{k}=\mathbf{0}$ and has nothing to do with such exchange of subbands. The Hartree effect is particularly crucial in wide quantum wells, in which holes are separately localized in two trianglelike confinement potentials near the side walls of the well due to the strong Hartree potential. In the extreme wide wells, the highest subband is fourfold degenerate, i.e., $HH1$ and $HH2$.

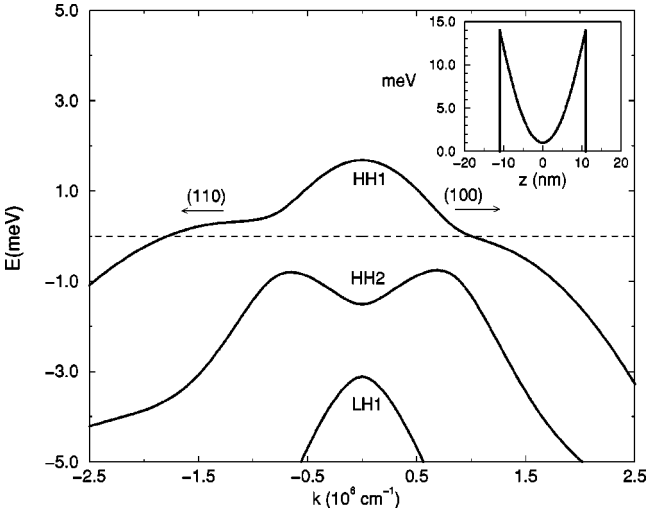

FIG. 5. Band structure for the symmetrically doped *p*-type $GaAs/Al_{0.37}Ga_{0.63}As$ quantum well with the same well width and density as those in Fig. 3 in (100) and (110) directions, calculated self-consistently from the $4\times 4\mathbf{k}\cdot\mathbf{p}$ model within the Hartree approximation. Dashed line: Fermi level, taken as energy zero. Inset: band-edge energy profile of the quantum well in Hartree approximation ($E_F=0$).

1. Single-subband approximation

First consider only the highest degenerate subband $HH1$ in the l and l' summations of Eq. (19). The calculated intrasubband dispersions in the long-wavelength range for q in both (100) and (110) directions are shown in Fig. 6(a). For isotropic cases, it has been shown in the preceding section that the intrasubband plasmons in the single-subband ap-

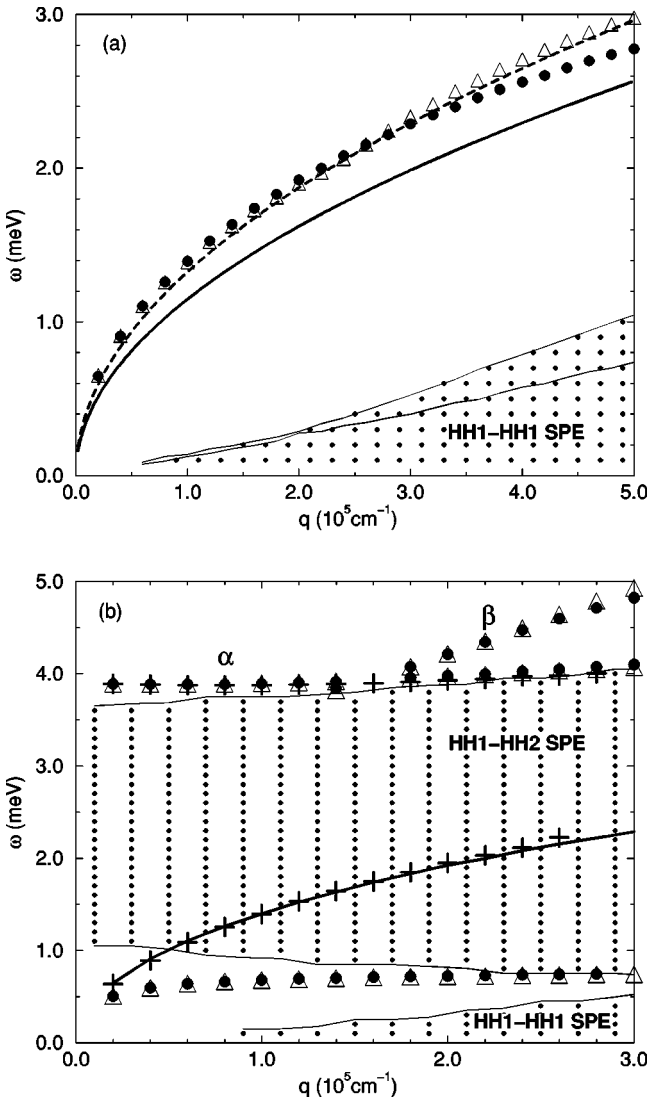

FIG. 6. Plasmon dispersions and SPE's for the sample of Fig. 5. (a) Intrasubband plasmon dispersions and SPE's, obtained by the calculation considering only highest subband $HH1$. Filled circles [empty triangles]: intrasubband plasmon dispersion for q in (100) [q in (110)]. Thick solid (dashed) line: ideal two-dimensional plasmon frequency, $\omega_p=(2\pi N_h e^2 q/\kappa m_p)^{1/2}$, with the effective plasmon mass $m_p=m_c(k_F)=1.2m_0$ ($m_p=0.9m_0$); see text. Hatched area: the intrasubband SPE. Thin solid lines: the extreme boundaries of intrasubband SPE region for q in (100) (upper) and q in (110) (lower). (b) Filled circles (empty triangles): intra- and intersubband plasmon modes for q in (100) [q in (110)], calculated with the two highest subbands ($HH1$,$HH2$). Plus symbols: overlap of wave functions neglected, see text. Solid line: intrasubband plasmon for q in (100), only highest subband $HH1$ considered, as shown in (a). Hatched area: the allowed inter- and intrasubband SPE.

proximation can be well approximated by the ideal 2D plasmon frequency of Eq. (30) with the effective plasmon mass replaced by the effective cyclotron mass near the Fermi energy.[19] For anisotropic two-dimensional systems, the ''cyclotron mass'' for the highest degenerate subband $HH1$ is defined by $m_c(E_F)\equiv\pi\hbar^2 D(E_F)$, where $D(E_F)$ is the density of states of degenerate subband $HH1$ at the Fermi energy.[27] We find that the intrasubband plasmons in this anisotropic system cannot be so well approximated by the ideal 2D plasmon frequency with $m_p=m_c(E_F)$ in Eq. (30) as those in isotropic cases. However, with the value slightly lighter than the cyclotron mass, $m_c(E_F)\approx 1.2m_0$, the extracted plasmon effective mass, $m_p\approx 0.9m_0$, is still in the same order as that of $m_c(E_F)$. It is also found that the effect of anisotropy of the plasmon dispersion is weak, at least for this sample, even though the band structure has a remarkable anisotropy, and only a minor difference between the plasmon dispersions in (100) and (110) directions can be noticed for $q>3\times10^5$ cm^{-1}.

2. Two-subband approximation

The results calculated in the two-subband ($HH1$ and $HH2$) approximation are shown in Fig. 6(b) as filled circles. The plasmon dispersion shown in Fig. 6(b) possesses the same basic characteristic of that in Fig. 4(b), which we have previously discussed in detail. But, the intersubband plasmons have *two* branches, instead of only one. Besides the β mode, the other mode, denoted as α, has a frequency depending only weakly on q in the long-wavelength limit and occurs also for $\mathbf{q}=\mathbf{0}$. It is difficult to obtain an analytical formulation like the analysis in Sec. III B 2 in this case, which involves more basis functions $\{f_n\}$. However, such a change of the plasmon feature in Fig. 6(b) is not surprising because the intersubband excitations between $HH1$ and $HH2$ have different selection rules from those between $HH1$ and $LH1$ for the case in Sec. III B 2. For instance, consider the vertical excitation between the states at the $HH1$ and $LH1$ subbands in the two-subband approximation in Sec. III B 2. The zero overlap of the $HH1$- and $LH1$-like states with the same $\mathbf{k}$ means that such vertical excitation cannot happen, regardless of the polarization of the incident light, because the inner product of the four-component vectors $\hat{c}^{(HH1,s),\mathbf{k}}$ and $\hat{c}^{(LH1,s),\mathbf{k}}$ is zero and these states have the same parity. In contrast, the excitations between the states in the $HH1$ and $HH2$ subbands, which do not have the same parity (but at $\mathbf{k}=\mathbf{0}$ the same $\hat{c}^{(HHn,s),\mathbf{0}}$) and cannot be represented only by a single basis function $f_1(z)$, are possible even for $\mathbf{q}=0$ if the incident light has proper polarization. Therefore, we do not attribute the α modes to the effect of finite overlap, like the β modes, but consider them as the usual intersubband excitation between $HH1$- and $HH2$-like states, similar to the intersubband excitations in electron quantum wells.

To check this point, we deliberately neglected this overlap in the polarizability, Eq. (19), by the replacements $[\hat{c}_m^{l,\mathbf{k}}]^\dagger\hat{c}_n^{l',\mathbf{k}+\mathbf{q}}\rightarrow[\hat{c}_m^{l,\mathbf{k}}]^\dagger\hat{c}_n^{l',\mathbf{k}}$ and $[\hat{c}_{m'}^{l',\mathbf{k}+\mathbf{q}}]^\dagger\hat{c}_{n'}^{l,\mathbf{k}}\rightarrow[\hat{c}_{m'}^{l',\mathbf{k}}]^\dagger\hat{c}_{n'}^{l,\mathbf{k}}$, but we did not neglect the $\mathbf{q}$ dependence in the Fermi function and the energy denominator. The plasmon dispersion calculated with this modification is shown by the plus symbols in Fig. 6(b). We find that the intersubband plasmon mode β disappears but the mode α still exists in this model. Furthermore, the intrasubband plasmons are now decoupled from the only surviving intersubband plasmon branch (α), and the depression of the frequencies of the intrasubband plasmons does not occur. Therefore, the coupling of the in-

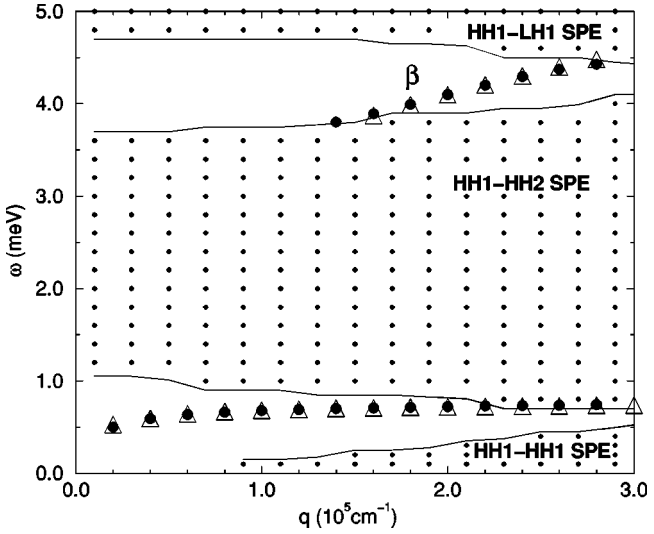

FIG. 7. Plasmon dispersions and SPE's, obtained by the calculation considering the three highest subbands $HH1$, $HH2$, $LH1$, for the same sample of Fig. 5. Filled circles [empty triangles]: the plasmon dispersion for q in (100) [q in (110)]. Hatched area: the allowed inter- and intrasubband SPE's.

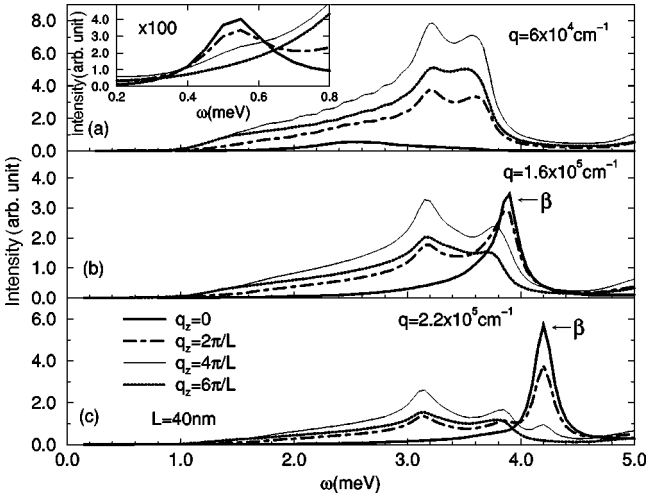

FIG. 8. Calculated energy-loss spectra for the sample of Fig. 5, whose plasmon dispersion is shown in Fig. 7, for various values of the wave vector $(\mathbf{q},q_z)$ of the externally applied longitudinal electric field.

trasubband plasmons to the intersubband plasmons has the same origin as the existence of the intersubband plasmon branch β, and can be attributed to the $\mathbf{k}$ dependence of valence subband wave functions, notably to the finite overlap of wave functions with different l and different $\mathbf{k}$ values.

3. Three-subband approximation

The existence of the intrinsic coupling in hole systems makes the inclusion of higher subbands in the plasmon calculation necessary. Figure 7 shows the plasmon dispersion obtained by the calculation, in which the three highest subbands $HH1$, $HH2$, and $LH1$ are included. We see that, due to the coupling of the $HH1$-$LH1$ excitations, the α branch is depressed into the region of SPE, and only the β branch is left in the gap between the edge of $HH1$-$LH1$ and $HH1$-$HH2$ SPE. The α mode therefore disappears in the diagram of plasmon dispersion. Nevertheless, we will see later that this Landau-damped mode is still observable in our calculated energy-loss spectra.

D. Absorption spectra

Figure 8 shows the calculated energy-loss spectra $\overline{P}_n/u_n$ for a Fourier component of the external electric field with wave vector $(\mathbf{q},q_z=k_n)$, for simplicity without the factor $2\kappa^2 v_{q_n}^{3d}$. The calculation includes the three highest degenerate subbands and is based on the results of Fig. 5. The damping parameter $\gamma=0.1$ meV is taken in Eq. (12). In Fig. 8(a), we see a broad absorption signal in the range of the SPE energies (1–3.8 meV) for $q=6\times10^4\text{cm}^{-1}$ and a local maximum near $\omega=3.6$ meV, the upper edge of the intersubband SPE energy. One also notices an absorption peak near $\omega=3.2$ meV, which we attribute to the Landau-damped intersubband plasmon mode α [see Figs. 6(b) and 7], merged in the absorption signal of the intersubband SPE. The absorption signal for the intrasubband plasmon is much weaker than those for intersubband plasmons and shown in the inset of Fig. 8(a). It is even weaker than the structureless absorption signal from the SPE continuum. Figure 8(b) shows the absorption spectra for $q=1.6\times10^5$ cm^{-1}. In Fig. 8(b), besides the absorption signal from the α mode, the absorption peak at the frequency $\omega\approx3.9$ meV due to the β mode is also observable but the peak partially overlaps with the SPE continuum. As q increases to $q=2.2\times10^5\text{cm}^{-1}$, as shown in Fig. 8(c), the strong β mode can be clearly distinguished from the signals of the SPE and α mode.

We also find that the intensity of absorption strongly depends on the Fourier component of the applied electric field. For the intrasubband plasmon and intersubband plasmon β, the strongest signal is obtained for the $q_z=0$ component, and the strength decays as q_z increases. The strongest absorption signal for the plasmon α results when the wavelength $\lambda_z=2\pi/q_z$ is comparable with the well thickness ($w=22$ nm), i.e., when $\lambda_z\approx w$. Thus, in Figs. 8(a), 8(b), and 8(c), the absorption signals for the α plasmon have the strongest intensity for $q_z\approx4\pi/L$($L=40$ nm, i.e., $\lambda_z=20$ nm), and decay as q_z becomes smaller or larger. According to such various q_z dependences, the minor signal near $\omega=2.5$ meV in Fig. 8(a), which is observable only for $q_z=0$, could be attributed to the strongly Landau-damped β mode. The strength of the absorption signals from the intersubband α and β plasmons have also different dependences on the magnitude of the in-plane $\mathbf{q}$ vector. As q increases, the absorption signals for the β plasmons become stronger but those for the α plasmons become weaker.

IV. SUMMARY

In conclusion, we have developed a theoretical approach to the calculation of collective excitations in hole quantum wells, which treats the nonparabolicity and the wave-vector

dependence of the subband wave functions within the $\mathbf{k}\cdot\mathbf{p}$ model exactly. We calculated the plasmon modes, single-particle excitations, and energy-loss spectra, and compared them to the electron quantum wells in detail. The calculated results show that there are two different intersubband plasmon modes for holes, and that inter- and intrasubband plasmons in the *p*-type quantum wells are intrinsically coupled, even though the structure of quantum wells has inversion symmetry. These couplings cause the effective plasmon masses to be heavier than the cyclotron masses. In the calculated energy-loss spectra, we find that intersubband plasmons have stronger absorption signals than intrasubband plasmons, and the intensity of the absorption signals is strongly dependent on the Fourier component of the incident electric field. In order to obtain the correct types of plasmon modes and selection rules for low-energy intersubband excitations, it was essential to include interaction effects also in the ground-state calculation, since, for sufficiently wide quantum wells, the Hartree potential changes the second valence subband from light- to heavy-hole-like.

To keep the discussion transparent, we neglected the exchange and correlation effect (which may affect the intersubband excitation energies) and presented explicit calculations only for symmetric quantum wells with sufficiently low hole density, so that only the highest valence subband is partially occupied. Asymmetric doping leads to asymmetric wells with a more complicated band structure, in which the spin degeneracy (at the same $\mathbf{k}\neq\mathbf{0}$) is lifted, so that always at least two hole subbands are occupied. The general formalism developed in this paper can, of course, also be applied to this more complex situation.

ACKNOWLEDGMENTS

The authors thank V. Latussek and A. Pfeuffer-Jeschke for helpful suggestions about $\mathbf{k}\cdot\mathbf{p}$ calculations. S.J.C. acknowledges support from the Deutscher Akademischer Austauschdiest (DAAD).

APPENDIX A: THE MATRIX ELEMENTS OF THE COULOMB INTERACTION WITHIN THE PLANE-WAVE FOURIER EXPANSION

It is straightforward to calculate within the plane-wave Fourier expansion the matrix elements

$$v^q_{m,n}=\frac{v_q}{L}\int_{-L/2}^{L/2}dz\int_{-L/2}^{L/2}dz'\,e^{-\imath k_m z}e^{-q|z-z'|}e^{\imath k_n z'} \quad \text{(A1)}$$

of the Green's function $W_q(z-z')$ in Eq. (13):

$$v^q_{m,n}=2qv_q\left[\frac{1}{q_m^2}\delta_{m,n}-(-1)^{m+n}\frac{1-e^{-qL}}{qL}\frac{q^2-k_mk_n}{q_m^2q_n^2}\right], \quad \text{(A2)}$$

where $k_m=2\pi m/L$ and $q_m^2=q^2+k_m^2$. Apparently the first diagonal term reestablishes the three-dimensional Fourier component of the Coulomb interaction, instead of the 2D form v_q. The second term describes edge effects due to the finite slab thickness L. Since the matrix in Eq. (A2) is separable, it is straightforward to calculate its inverse. With the restriction $|m|\leqslant M$, we have a square matrix of dimension $2M+1$. For the inverse matrix we obtain

$$[v^{-1}(q)]_{m,n}=\frac{1}{2qv_q}\left[q_m^2\delta_{m,n}+\frac{2(-1)^{m+n}}{qL}\times(\alpha_M q^2-\beta_M k_m k_n)\right], \quad \text{(A3)}$$

with the prefactors $\alpha_M(y)=1/[1+r_M(y)]$ and $\beta_M(y)=1/[1+r_M(y)+(2M+1)/(\pi y)]$, where $y=qL/(2\pi)$ and $r_M(y)=(2/\pi)\mathrm{Im}\,\psi(M+1+\imath y)$. Here $\psi(z)$ is the digamma function, and we have used the identity[28]

$$\sum_{m=1}^{M}\frac{y}{m^2+y^2}=\frac{\pi}{2}\coth(\pi y)-\frac{1}{2y}-\mathrm{Im}\,\psi(M+1+\imath y), \quad \text{(A4)}$$

which holds for real y and yields for $M\gg 1$

$$\frac{\pi}{2}r_M(y)\approx\arctan\frac{y}{M+1}+\frac{1}{2}\frac{y}{(M+1)^2+y^2}+\frac{1}{6}\frac{y(M+1)}{[(M+1)^2+y^2]^2}+\cdots. \quad \text{(A5)}$$

APPENDIX B: APPROXIMATE DIELECTRIC FUNCTION IN THE TWO-SUBBAND ($HH1$ AND $LH1$) MODEL

If the two highest valence subbands in a hole quantum well are $HH1$- and $LH1$-like, an approximate *scalar* dielectric function can be derived in the two-subband ($HH1$ and $LH1$) approximation. This is very different from the case of electron quantum wells, where the orthogonality of the subband wave functions of adjacent subbands results from the z-dependence, which leads to the dielectric matrix in the excitation basis (Sec. II B 1). In the present case, the Hamiltonian [Eq. (2)] is diagonal at $\mathbf{k}=\mathbf{0}$ and the eigenfunctions have, according to Eq. (1), the structure $\hat{\Psi}_{l,\mathbf{k}=\mathbf{0}}(z)=\phi_l(z)\hat{c}^{l,\mathbf{0}}$, with only a single nonzero component of the four-vectors $\hat{c}^{l,\mathbf{0}}$ and with slightly different basis sets $\{\phi_{HHn}(z)\}$ and $\{\phi_{LHn}(z)\}$ for heavy- $[l=(HHn,s)]$ and light- $[l=(LHn,s)]$ holes states, respectively, where s is spin. For infinitely high valence-band offset, these basis sets would be identical, and for realistic band offsets at least the $n=1$ (cosinelike) functions $\phi_{HH1}(z)\approx\phi_{LH1}(z)$ are nearly equal. At finite $\mathbf{k}$, we find that the wave functions of the two uppermost hole subbands are a hybridization of mainly $\hat{\Psi}_{(HH1,s),\mathbf{0}}(z)$ and $\hat{\Psi}_{(LH1,s'),\mathbf{0}}(z)$, with only small admixture of higher $(n>1)$ subbands, and can be well approximated by

$$\hat{\Psi}_{l,\mathbf{k}}(z)\approx f_1(z)\hat{c}_1^{l,\mathbf{k}}, \quad \text{(B1)}$$

with the same (normalized) function $f_1(z)=\phi_{HH1}(z)=\phi_{LH1}(z)$ for $l=(HH1,s)$ and $(LH1,s')$. Thus, the overlap

$$\langle l,\mathbf{k}|l',\mathbf{k}'\rangle = \int dz[\hat{\psi}_{l,\mathbf{k}}]^{\dagger}(z)\hat{\psi}_{l',\mathbf{k}'}(z) = [\hat{c}_1^{l,\mathbf{k}}]^{\dagger}\hat{c}_1^{l',\mathbf{k}'} \tag{B2}$$

reduces to the scalar product of the four-vectors $\hat{c}_1^{l,\mathbf{k}}$, and the overlap for $\mathbf{k}'=\mathbf{k}$ and $l'\neq l$ vanishes due to the orthogonality of the $\hat{c}_1^{l,\mathbf{k}}$, not due to the z dependence of the wave functions as in electron quantum wells. As a consequence, no vertical ($\mathbf{k}'=\mathbf{k}$) intersubband excitations between the uppermost heavy- and light-hole subbands are possible, since, due to the factorization [Eq. (B1)], the corresponding intersubband matrix element will be zero, whatever the polarization of the incident light may be. Evaluating the dielectric tensor with the ansatz Eq.(B1) in Eqs. (17)–(19), we obtain the scalar dielectric function of Eq. (31).

[1] D. Heitmann, J. P. Kotthaus, and E. G. Mohr, Solid State Commun. **44**, 715 (1982).
[2] D. Olego, A. Pinczuk, A. C. Gossard, and W. Wiegmann, Phys. Rev. B **25**, 7867 (1982).
[3] A. Pinczuk and J. M. Worlock, Physica B **117&118B**, 637 (1983).
[4] R. Sooryakumar, A. Pinczuk, A. Gossard, and W. Wiegmann, Phys. Rev. B **31**, 2578 (1985).
[5] S. Oelting, D. Heitmann, and J. P. Kotthaus, Phys. Rev. Lett. **56**, 1846 (1986).
[6] E. Batke, D. Heitmann, A. D. Wieck, and J. P. Kotthaus, Solid State Commun. **46**, 269 (1983).
[7] C. Schüller, J. Kraus, V. Latussek, and J. K. Ebeling, Solid State Commun. **81**, 3 (1992).
[8] C. Schüller, J. Kraus, G. Schaack, G. Weimann, and K. Panzlaff, Phys. Rev. B **50**, 18 387 (1994).
[9] A. G. Rojo, J. Phys.: Condens. Matter **11**, R31 (1999).
[10] C. Jörger, S. J. Cheng, W. Dietsche, R. Gerhardts, P. Specht, K. Eberl, and K. v. Klitzing, Physica E (Amsterdam) **6**, 598 (2000); C. Jörger, S. J. Cheng, H. Rubel, W. Dietsche, R. Gerhardts, P. Specht, K. Eberl, and K. v. Klitzing, Phys. Rev. B **62**, 1572 (2000).
[11] B. Vinter, Phys. Rev. B **15**, 3947 (1977).
[12] T. Ando, A. B. Fowler, and F. Stern, Rev. Mod. Phys. **54**, 437 (1982).
[13] S. Das Sarma, Phys. Rev. B **29**, 2334 (1984).
[14] J. K. Jain and S. Das Sarma, Phys. Rev. B **36**, 5949 (1987).
[15] D. A. Broido and K. Kempa, Phys. Rev. B **41**, 3268 (1990).
[16] M. Zalużny, Phys. Rev. B **49**, 2923 (1994).
[17] G. Bastard and J. A. Brum, IEEE J. Quantum Electron. **QE-22**, 1625 (1986).
[18] W. Schmitt, Phys. Rev. B **50**, 15 221 (1994); Ph.D. thesis, University of Würzburg (1993).
[19] S. J. Cheng and R. R. Gerhardts, Solid State Commun. **116**, 669 (2000).
[20] H. Ehrenreich and M. H. Cohen, Phys. Rev. **115**, 786 (1959).
[21] J. M. Luttinger, Phys. Rev. **102**, 1030 (1956).
[22] M. Altarelli, U. Ekenberg, and A. Fasolino, Phys. Rev. B **32**, 5138 (1985).
[23] V. Latussek, E. Bangert, and G. Landwehr, Ann. Phys. (Leipzig) **48**, 394 (1991).
[24] L. R. Ram-Mohan, K. H. Yoo, and R. L. Aggarwal, Phys. Rev. B **38**, 6151 (1988).
[25] J. D. Jackson, *Classical Electrodynamics* (Wiley, New York, 1975).
[26] G. E Marques and V. A. Chitta, J. Phys. C **20**, L727 (1987).
[27] D. A. Broido and L. J. Sham, Phys. Rev. B **31**, 888 (1985).
[28] *Handbook of Mathematical Functions*, edited by M. Abramowitz and I. A. Stegun (Dover, New York, 1972).